



AuPd/3DOM-TiO₂ catalysts for photocatalytic reduction of CO₂: High efficient separation of photogenerated charge carriers



Jinqing Jiao^{a,1}, Yuechang Wei^{a,*1}, Yilong Zhao^a, Zhen Zhao^{a,b,*}, Aijun Duan^a, Jian Liu^a, Youyong Pang^a, Jianmei Li^a, Guiyuan Jiang^a, Yajun Wang^a

^a State Key Laboratory of Heavy Oil Processing, China University of Petroleum-Beijing, Chang Ping, Beijing 102249, China

^b Institute of Catalysis for Energy and Environment, Shenyang Normal University, Shenyang 110034, China

ARTICLE INFO

Article history:

Received 11 January 2017
Received in revised form 25 February 2017
Accepted 27 February 2017
Available online 28 February 2017

Keywords:

3DOM materials
TiO₂
AuPd nanoparticles
Photocatalysis
CO₂ conversion

ABSTRACT

The photocatalytic conversion of CO₂ and H₂O into value-added chemicals using sunlight is significant to solve energy crisis and environmental problems. In this work, a series of novel bifunctional catalysts of core-shell structured AuPd nanoparticles decorated 3DOM TiO₂ (AuPd/3DOM-TiO₂) were successfully fabricated via a facile one-pot method of gas bubbling-assisted membrane reduction (GBMR). AuPd/3DOM-TiO₂ catalysts show uniform 3D ordered macroporous structure, and the slow photon effect of 3DOM-TiO₂ as a photonic crystal can enhance light-harvesting efficiency. AuPd nanoparticles are highly dispersed on the surface of 3DOM-TiO₂ carrier. Since bimetallic AuPd nanoparticles with the relatively low Fermi level have good capacity of trapping electron, they can efficiently promote the separation of photogenerated electron-hole pairs in TiO₂. The AuPd/3DOM-TiO₂ catalysts exhibit excellent photocatalytic activity for CO₂ reduction with H₂O to CH₄ under light irradiation. Among the studied catalysts, Au₃Pd₁/3DOM-TiO₂ catalyst exhibits the highest photocatalytic activity and selectivity for CO₂ reduction, e.g., its formation rate of CH₄ is 18.5 μmol g⁻¹ h⁻¹ and its selectivity to CH₄ production by CO₂ reduction is 93.9%. The possible mechanism of AuPd/3DOM-TiO₂ catalysts for photocatalytic CO₂ reduction is also proposed, and it would guide further design and synthesis of high efficient photocatalysts for CO₂ reduction with H₂O.

© 2017 Elsevier B.V. All rights reserved.

1. Introduction

For the past few years, the photocatalysis technology of utilizing solar energy to convert CO₂ into highly valuable organic compounds (e.g. CH₃OH and CH₄) has been investigated [1,2]. The artificial conversion of CO₂ with H₂O to produce fuels and chemicals using solar light could not only remit the global warming problem but also provide the development of new renewable fuels [3,4]. Since the pioneering researches reported by Fujishima [5], a variety of scientific researchers have been devoted to the fabrications of high efficient photocatalysts for CO₂ reduction with H₂O [6–8]. In the process of photocatalytic CO₂ conversion, the well-developed characteristics of efficient semiconductor-based photocatalysts, for instance, the suitable band gap and the efficiency photogenerated charge separation and migration, play a certain critical role [9–12].

Among the reported photocatalysts, titanium dioxide (TiO₂) is recognized as the most widely investigated photocatalysts because of its nontoxicity, cost inexpensive, corrosion resistant, and physical and chemical stability [13–16]. However, there are two major drawbacks of TiO₂ including the weak absorption to visible light irradiation and the fast recombination of photo-generated charges [17,18]. In order to enhance the light-harvesting efficiency and the separation efficiency of photon-generated charge carriers, numerous strategies, such as metal cation and anions doping [19–21], crystal engineering [22,23], surface sensitization [24], metal deposition [25,26], fabrication of heterojunctions by combination with secondary semiconductors [27,28], have been proposed to improve photocatalytic performance for CO₂ reduction.

For improving the light-harvesting efficiency of TiO₂, three-dimensionally ordered macroporous (3DOM) materials, also named as inverse opals, have been demonstrated to significantly enhance the light absorption and improve the light energy conversion efficiency as well [29–31]. The periodic structure of 3DOM materials can forbid the propagation of light by the band gap scattering effect, increase the path length of light through slow-light effect and result in a stop-band reflection because of coherent Bragg

* Corresponding authors at: 18# Fuxue Road, Chang Ping District, Beijing, 102249, China.

E-mail addresses: weiyi@cup.edu.cn (Y. Wei), zhenzhao@cup.edu.cn (Z. Zhao).

¹ These authors contributed equally to this work.

diffraction [32,33]. Moreover, the periodicity and dielectric contrast of 3DOM materials are dependent on the stop-band reflection frequencies [34]. In our previous works [35,36], it has been found that the corresponding photonic stop-band edge matching with the irradiation wavelength can be adjusted by the pore sizes of 3DOM TiO₂, and the exact overlap between stop-band and the electronic absorption band of the material can notably improve the light-harvesting efficiency in the visible light, which results in the enhancing photocatalytic activity for CO₂ reduction with H₂O.

The heterojunction structure of photocatalysts has been considered as an excellent strategy to retard charge recombination and significantly enhance the overall photocatalytic activity [37,38]. Due to the states of its Fermi levels below the conduction band edge of TiO₂ energetically, thus, photogenerated electrons in the conduction band (CB) of TiO₂ can be rapidly transferred and trapped on the surface of noble metals [39,40]. Noble metals serving as a reservoir of photoelectrons, could suppress the recombination of photoexcited electron-hole pairs and improve the quantum efficiency of photocatalytic reactions [41,42]. The Schottky barrier formed at heterojunction interface can further prevent electron-hole recombination due to the internal electric field. Moreover, some noble metal (Au, Ag etc) can facilitate the absorption efficiency in the visible region because of their extraordinary localized surface plasmon resonance (SPR) [43]. It has been demonstrated that bimetallic nanoparticles (NPs, such as AgPd, AuPt) deposition could improve catalytic performances compared with monometallic NPs [44,45]. For the sake of the maximum atom efficiency of noble metals, many methods have been employed to effectively control the dispersion and size of noble metals anchored on supports [46,47]. However, it is still challenge to fabrication of fine structured photocatalysts with well dispersion and high separation efficiency of photon-generated carriers.

Herein, a series of 3DOM TiO₂-supported core-shell structured AuPd NPs (AuPd/3DOM-TiO₂) were designed and fabricated by a facile one-pot method of gas bubbling-assisted membrane reduction-precipitation (GBMR). The GBMR method could efficiently control the nucleation and growth of noble metal particles through control the adding rate and dispersion of reductant reagent. The Pd shell is coated selectively on the surface of Au NPs to form a Pd-Au-TiO₂ heterostructure nanocrystal on the surface of 3DOM-TiO₂, which improve the transfer efficiency of photogenerated charges and the subsequent photocatalysis. The photocatalysts of AuPd/3DOM-TiO₂ exhibit superior catalytic activity for CO₂ reduction under light irradiation. The photocatalytic mechanism of AuPd/3DOM-TiO₂ for CO₂ reduction was discussed and elaborated.

2. Experimental section

2.1. Synthesis of materials

3DOM-TiO₂ support was synthesized by the method of colloidal crystal template (CCT). The synthesis procedures, such as preparations of monodispersed polymethyl methacrylate (PMMA) microspheres, fabrication of CCT via centrifugation method, and assembly, have been described and reported in the previous papers [48–50]. 3DOM-TiO₂ support was obtained after calcination at 600 °C for 5 h in a tube furnace.

A series of bimetallic AuPd nanoparticle catalysts (weight ratios of Au/Pd=3, 1, and 1/3) were prepared by one-pot process of GBMR method with the poly(N-vinyl-2-pyrrolidone) (PVP) as the protecting agent and NaBH₄ as the reducing agent. The detailed information about the gas bubbling-assisted membrane reduction apparatus and schematic diagram are described previously [51,52]. The total noble metal content of photocatalyst is 4.0 wt%. The typical preparation processes are described as follows: Firstly, 3DOM

TiO₂ support (1 g) was added into 100 mL deionized water and then a desired amount of protecting agent (PVP) was dropped under vigorous stirring. Subsequently, the aqueous solution of HAuCl₄ and PdCl₂ with the theoretical weight ratios of Au/Pd being 3, 1 and 1/3 was added into the before-mentioned mixing solution. After vigorously stirred for 0.5 h, the mixture flowed into the ceramic membrane reactor driven by a peristaltic pump. And NaBH₄ solution (the mole ratio of NaBH₄/noble metal is 5) driven by a constant flow pump was injected into the membrane reactor and incorporated with the metal precursor mixed solution through the holes (d=40 nm) on the ceramic membrane tubes. In order to make before-mentioned mixing solution homogenous, in the meantime, hydrogen gas was introduced into the membrane reactor via the other two ceramic membrane tubes. After completing the consumption of NaBH₄ solution, the reaction system was further vigorously bubbled with hydrogen gas for 1 h. Then, AuPd/3DOM-TiO₂ catalysts were obtained after filtered, washed, dried and calcined at 400 °C for 2 h. For comparison, Au/3DOM-TiO₂ and Pd/3DOM-TiO₂ catalysts with the same total metal loading were also prepared in similar process.

2.2. Characterization

The morphology and microscopic structure information were obtained on a scanning electron microscope (SEM, FEI Quanta 200F) and a transmission electron microscope (TEM, JEOL JEM 2100) equipped with a field emission source at an accelerating voltage of 200 kV. Mercury intrusion porosimetry (MIP) experiments were performed by a Micromeritics AutoPoreIV 9500 apparatus. The specific surface area was calculated by the Brunauer-Emmett-Teller (BET) method. The crystal phase properties of all as-prepared samples were analyzed with a powder X-ray diffractometer (Shimadzu XRD 6000) and a Renishaw Micro-Raman System 2000 spectrometer. The laser line of Raman microscope was 532 nm. X-ray photoelectron spectra (XPS) were acquired by a Perkin-Elmer PHI-1600 ESCA spectrometer with Mg Kα emission. The actual contents of Au and Pd were determined by inductive coupled plasma atomic emission spectrometry (ICP-AES). Photoluminescence (PL) spectra were recorded using the Edinburgh Instruments Xe900 equipped with a Xe lamp and the excitation wavelength was set at 380 nm. The surface photovoltage (SPV) measurements were carried out on a surface photocurrent spectroscope (PL-SPS/IPCE1000). Photoelectrochemical (PEC) measurements were performed on an electrochemical workstation (CHI660E) in the saturated solution of Na₂SO₄, which has a three-electrode configuration and all as-prepared samples, the saturated Ag/AgCl, a platinum foil were employed to as working photoelectrode, reference and counter electrode, respectively. And PEC measurements assigned to CO₂ reduction were also performed on the same equipment in NaHCO₃ solution (0.1 mol L⁻¹). The potential of -0.6 V (vs. SCE) was applied to the work electrode. Before the experiment, CO₂ was purged into NaHCO₃ solution for 20 min until it was saturated. The samples were illuminated under a 300 W Xe lamp.

2.3. Photocatalytic reduction of CO₂

CO₂ photocatalytic reduction was carried out in a gas-closed circulation system (Perfect Light Company, Beijing, China) irradiated under a 300 W Xe lamp (λ=320–780 nm). The certain amount of catalysts was uniformly dispersed on a watch-glass with the basal diameter of 6.5 cm. Before the light irradiation, the photoreactor system was thoroughly vacuum-treated, then CO₂ gas was introduced into the circulation system. The deionized water (2 mL) was injected into the bottom of the reactor. The intensity of incident light was measured to be 80 mW cm⁻² by a spectroradiometer. During the light irradiation in 6 h, the amounts of H₂, CO, and

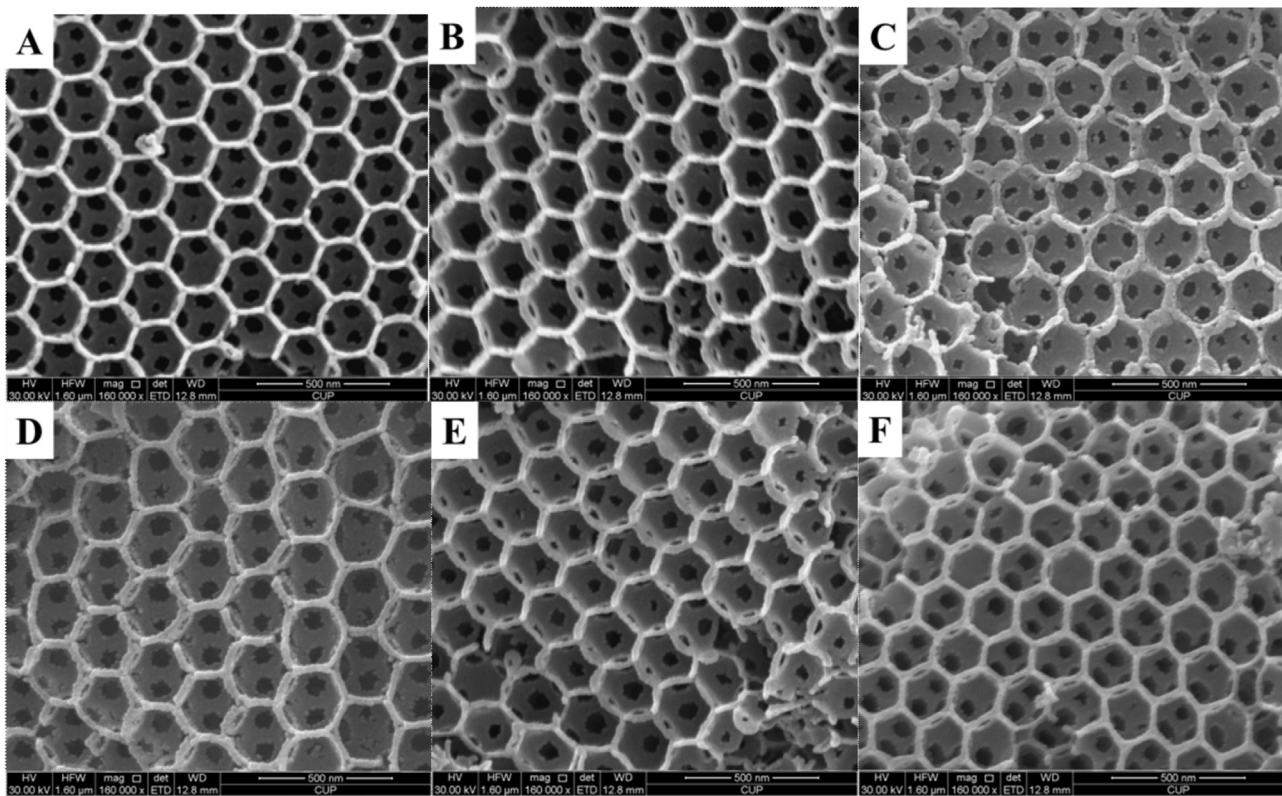


Fig. 1. SEM images of 3DOM-TiO₂ and AuPd/3DOM-TiO₂ catalysts. A. TiO₂; B. Au₄/3DOM-TiO₂; C. Au₃Pd₁/3DOM-TiO₂; D. Au₂Pd₂/3DOM-TiO₂; E. Au₁Pd₃/3DOM-TiO₂; F. Pd₄/3DOM-TiO₂.

hydrocarbons in the reactor were analyzed by an online gas chromatograph (GC-9560; HuaAiSePu Corp., Shanghai, China) with a flame ionization detector (FID) and a thermal conductivity detector (TCD) each 40 min intervals. The gas products were analyzed by the external standard method. The apparent quantum efficiency (AQE) was measured under the similar photocatalytic reaction condition, and the irradiation light with different wavelength (380, 420, 450, 520 and 600 nm) using a band-pass filter (full width at half maximum 15 nm) was used as the light source. The incident flux was determined by Radiometer (FZ-A, Photoelectric Instrument Factory of Beijing Normal University). The AQE values of the CO₂ reduction were calculated according to the following Eq.:

$$\text{AQE} [\%] = \frac{\text{Number of Reacted Electrons}}{\text{Number of Incident Photons}} \\ = \frac{\text{Number of } \text{CH}_4 \times 8 + \text{Number of } \text{CO} \times 2}{\text{Number of Incident Photos}} \times 100\%$$

3. Results

3.1. The results of SEM images

In order to observe the morphology and macroporous structure of AuPd/3DOM-TiO₂ catalysts, SEM observations were carried out. Fig. 1 shows the SEM images of as-prepared catalysts with different weight ratios of Au/Pd obtained via one-pot GBMR method. The catalysts show clearly three-dimensionally highly ordered macroporous structure obtained via replicating of 3D close-packed PMMA template with a face-centered cubic (FCC) array [53]. The diameters of periodic voids are in the range of 200 ± 10 nm, which corresponds to shrinkage of 15–20% in comparison with the initial size

(250 nm) of PMMA microspheres (Fig. S1). The shrinkage may be caused by the melting of polymer templates and the formation of produced metal oxides. Moreover, the sublayer pores with relatively small sizes (60 ± 10 nm) can be observed clearly and connect the periodic voids, which could be helpful for the reactant diffusion and light harvesting. In addition, the morphology structure of AuPd/3DOM-TiO₂ catalysts (Fig. 1B-1F) is similar as that of 3DOM-TiO₂ (Fig. 1A), suggesting that the preparation process of supported bimetallic AuPd nanoparticles via GBMR method has not destroyed the ordered macroporous structure.

3.2. The results of mercury intrusion porosimetry (MIP)

The pore sizes of typical AuPd/3DOM-TiO₂ catalysts were further evaluated by means of mercury intrusion porosimetry (MIP) and the results are shown in Fig. 2. The peak value of the curve is corresponded to the diameter of the largest proportion of pores in catalysts. As exhibited in Fig. 2, the distribution of pore sizes in all catalysts is very narrow in the range of 20–250 nm, and the peak value corresponding to the most probable pore diameter is 65 nm in accordance with the results of SEM images. And the porosities, the average pore diameters, the total pore volumes and the pore area of AuPd/3DOM-TiO₂ catalysts analyzed by MIP are listed in Table 1. The pore volumes of 3DOM-TiO₂ and AuPd/3DOM-TiO₂ catalysts are about 2.3 mL g⁻¹, but the total pore volumes determined by N₂ physisorption are only 0.14 mL g⁻¹ (Table 1), indicating that the macropores are main contribution to the total porosity. The pore diameters of 3DOM-TiO₂ and AuPd/3DOM-TiO₂ catalysts are 200 ± 10 nm, which is in agreement with the value estimated from the SEM images. And the porosities (90%) are larger than the theoretical value (74%) of sphere volume in FCC array, which may be as a result of the shrinkage of oxide framework in the process of calcination [51]. In addition, the surface areas of all catalysts

Table 1

Porosities, average diameters, pore volumes and pore areas of typical 3DOM-TiO₂ and AuPd/3DOM-TiO₂ catalysts.

| Catalyst | $V_{N_2}^a$ (ml g ⁻¹) | V_{Hg}^b (ml g ⁻¹) | A_p^c (m ² g ⁻¹) | D_p^d (nm) | Porosity ^e (%) |
|--|-----------------------------------|----------------------------------|---|--------------|---------------------------|
| 3DOM-TiO ₂ | 0.14 | 2.3 | 45.8 | 201 | 90.5 |
| Au ₃ Pd ₁ /3DOM-TiO ₂ | 0.13 | 2.2 | 45.2 | 195 | 89.6 |
| Au ₂ Pd ₂ /3DOM-TiO ₂ | 0.13 | 2.2 | 43.6 | 202 | 90.1 |

^a Pore volume determined by BET method.

^b Total pore volume for pores.

^c Total pore area determined by Hg porosimetry.

^d The average pores diameter.

^e Determined by Hg porosimetry.

Table 2

The crystal parameters and average crystal sizes of 3DOM-TiO₂ and AuPd/3DOM-TiO₂ catalysts.

| Catalyst | D^a of TiO ₂ (nm) | AuPd size ^b (nm) | S_{BET}^c (m ² g ⁻¹) | Au content ^d (wt%) | Pd content ^d (wt%) |
|--|--------------------------------|-----------------------------|---|-------------------------------|-------------------------------|
| 3DOM-TiO ₂ | 20.6 | — | 58 | — | — |
| Au ₄ /3DOM-TiO ₂ | 21.1 | 3.3 | 59 | 3.4 | — |
| Au ₃ Pd ₁ /3DOM-TiO ₂ | 19.9 | 3.6 | 60 | 2.6 | 1.0 |
| Au ₂ Pd ₂ /3DOM-TiO ₂ | 20.5 | 3.9 | 59 | 1.7 | 1.8 |
| Au ₁ Pd ₃ /3DOM-TiO ₂ | 20.8 | 3.8 | 59 | 0.9 | 2.6 |
| Pd ₄ /3DOM-TiO ₂ | 20.6 | 4.2 | 60 | — | 3.3 |

^a Determined by XRD using Scherrer equation with the intensity of the most prominent peak, (101).

^b Determined by HRTEM.

^c Surface area obtained by BET method.

^d Determined by ICP-AES.

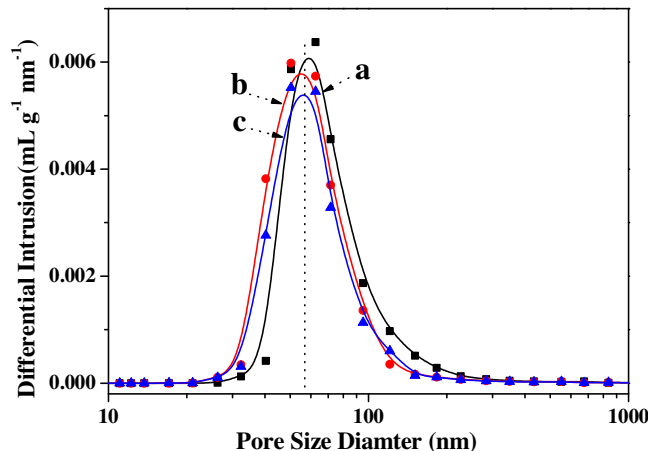


Fig. 2. The pore size distributions of typical 3DOM-TiO₂ and AuPd/3DOM-TiO₂ determined by MIP. a. 3DOM-TiO₂; b. Au₃Pd₁/3DOM-TiO₂; c. Au₂Pd₂/3DOM-TiO₂.

are also summarized in Table 2. The surface areas of 3DOM-TiO₂ and AuPd/3DOM-TiO₂ catalysts are in the range of 59 ± 1 m² g⁻¹. Moreover, according to the result of ICP-AES in Table 2, the weight percent of Au or Pd (Au, Pd) to TiO₂ and the weight ratios of Pd/Au are identical to the theoretical values, suggesting that GBMR method is an effective way to fabricate noble metals-support heterogeneous catalyst.

3.3. The results of XRD characterization

The phase structures of 3DOM-TiO₂ and AuPd/3DOM-TiO₂ catalysts were investigated by means of XRD characterization, and the results are presented in Fig. 3. It is shown that there are seven remarkably diffraction peaks (θ) centered at 25.4, 37.9, 48.1, 53.9, 55.2, 62.8 and 75.1 ° which can be assigned to the (101), (004), (200), (105), (211), (204) and (215) lattice planes of 3DOM-TiO₂ with the tetragonal phase structure of anatase type (PDF# 21-1272). Besides, the two weak diffraction peaks (θ) centered at 27.4 and 36.1 ° were also observed, which can be indexed to (110) and (101) crystal faces of 3DOM-TiO₂ with the tetragonal phase structure

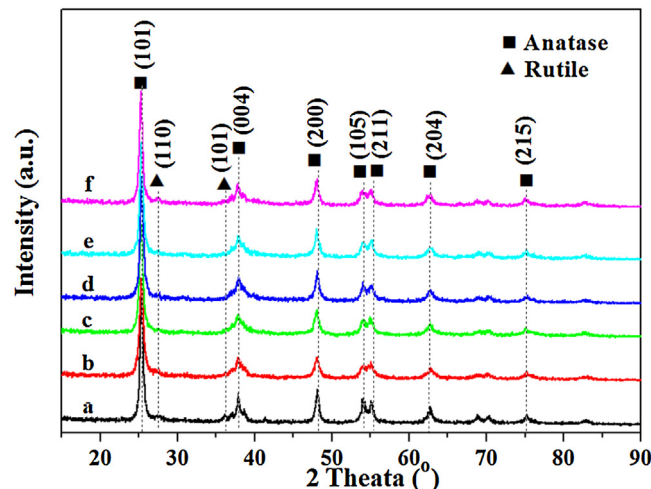


Fig. 3. XRD patterns of 3DOM-TiO₂ and AuPd/3DOM-TiO₂ catalysts. a. TiO₂; b. Au₄/3DOM-TiO₂; c. Au₃Pd₁/3DOM-TiO₂; d. Au₂Pd₂/3DOM-TiO₂; e. Au₁Pd₃/3DOM-TiO₂; f. Pd₄/3DOM-TiO₂.

of rutile type (PDF# 65-0191). It indicates that the crystal phase structures of anatase and rutile types are coexistent in 3DOM-TiO₂ support, which is similar to the crystal phase structure of commercial P25 (Fig. S2). It is well known that the coexistence of the anatase/rutile crystal phases can form the heterojunction of anatase/rutile phases, which would be helpful for enhancing the separation of photo-generated carriers and the photocatalytic activity. After introduction of supported AuPd NPs, the diffraction peaks belonging to 3DOM-TiO₂ did not change, and the characteristic diffraction peaks of AuPd NPs were not detected. The above-mentioned results indicate that the sizes or loadings of supported AuPd NPs are smaller than the detection limit of XRD spectra for supported nanoparticles. In addition, the average crystalline sizes of 3DOM-TiO₂ are determined by Scherer equation using the (101) diffraction peak, and the results are shown in Table 2. Their average crystalline sizes are about 20.0 nm. The wall thickness observed from SEM images was about 30 ± 5 nm (Fig. 1), thus, the macroporous wall seem to be composed of 1–3 crystallites.

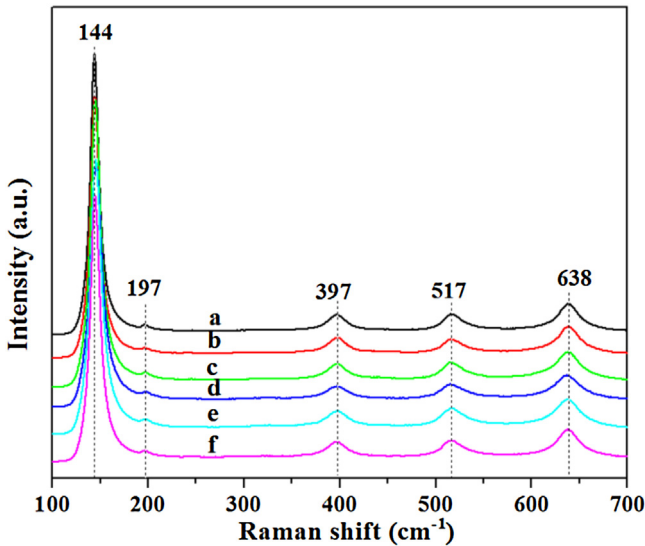


Fig. 4. Raman spectra of 3DOM-TiO₂ and AuPd/3DOM-TiO₂ catalysts. a. TiO₂; b. Au₄/3DOM-TiO₂; c. Au₃Pd₁/3DOM-TiO₂; d. Au₂Pd₂/3DOM-TiO₂; e. Au₁Pd₃/3DOM-TiO₂; f. Pd₄/3DOM-TiO₂.

3.4. The results of Raman spectroscopy characterization

The phase structures of 3DOM-TiO₂ and AuPd/3DOM-TiO₂ catalysts were further confirmed by Raman spectra and the results are shown in Fig. 4. In the case of 3DOM-TiO₂ samples, the four peaks centered at 144, 397, 517, and 638 cm⁻¹ can be attributed to the Raman-active modes of anatase phase with the symmetries of Eg, B1g, A1g, and Eg, respectively [54]. The peaks appeared at 144 cm⁻¹ is derived from the bending vibration of O-Ti-O bond, while the another three peaks are related to the Ti-O-Ti bending type [55]. The weak Raman peaks at 197 cm⁻¹ can be assigned to Raman-active modes of rutile phase. All these peaks reveal the coexistence of two crystal phases' structure in 3DOM TiO₂, which is in accordance with the results of XRD. After introduction of bimetallic AuPd NPs decorating on the surface of 3DOM-TiO₂, the Raman spectra are identical to that of 3DOM-TiO₂ support, and the related signals of AuPd NPs were not detected, because of the ultrafine particle size of NPs and the weak Raman scattering of these metals. Thus, based on the above results of XRD and Raman, it could be concluded that the deposition of AuPd NPs on the inner wall of 3DOM TiO₂ oxide makes less impact on the crystalline phase and crystallinity.

3.5. The results of TEM and HAADF-STEM images

Fig. 5 displays the TEM and HRTEM images of AuPd/3DOM-TiO₂ catalysts. As shown in Fig. 5A, 5C and 5E, it is observed that the catalysts have the ordered macroporous structure with overlapped pores in accordance with their SEM observation. Moreover, a mass of AuPd NPs are highly dispersed and uniform in size on the surface of 3DOM-TiO₂ (Fig. 5B, 5D and 5F). The uniform size and high dispersion of AuPd NPs may be helpful to increase the interaction between noble metals and TiO₂ support and effectively enhance the separation of photogenerated charges. The size distribution of supported bimetallic AuPd NPs is in the range of 2–6 nm, and the average diameter is about 3.7 ± 0.2 nm via statistical analyses of more than 100 AuPd NPs (Table 2). And one spherical Au₂Pd₂ NPs supported on the surface of TiO₂ exhibits clearly the lattice fringes with the plane spacing of 0.23 nm in inset of Fig. 5D, which is assigned to FCC(111) crystal faces of AuPd NPs. It indicates that supported AuPd NPs are crystalline, and there is a tight junction

Table 3

Surface compositions and charge states of Au and Pd species derived from XPS analyses.

| Sample (3DOM) | Au species (%) | | | | Pd species (%) | | | |
|--|-----------------|-----------------|------------------|----------------------------------|-----------------|------------------|------------------|----------------------------------|
| | Au ⁰ | Au ⁺ | Au ³⁺ | Au ^{&+^a} | Pd ⁰ | Pd ²⁺ | Pd ⁴⁺ | Pd ^{&+^a} |
| Au ₄ /3DOM-TiO ₂ | 73.8 | 19.0 | 7.2 | 26.2 | — | — | — | — |
| Au ₃ Pd ₁ /3DOM-TiO ₂ | 68.2 | 22.9 | 8.9 | 31.8 | 71.0 | 20.1 | 8.9 | 29.0 |
| Pd ₄ /3DOM-TiO ₂ | — | — | — | — | 52.2 | 31.6 | 16.2 | 37.8 |

^a The Au^{&+} (Pd^{&+^a}) values are equal to the sum of Au⁺ (Pd²⁺) and Au³⁺ (Pd⁴⁺).

between TiO₂ and supported AuPd NPs, which is beneficial to electron transfer from TiO₂ to AuPd NPs.

Fig. 6 show the HAADF-STEM and EDS elemental mapping images of Au₃Pd₁/3DOM-TiO₂ catalyst. As shown in Fig. 6A, supported Au₃Pd₁ NPs are homogeneously dispersed on the surface of 3DOM-TiO₂ supports, which is in agreement with the result of TEM images. The structure of supported Au₃Pd₁ NPs is further observed by means of HAADF-STEM-EDS elemental mapping in Fig. 6B. It obviously exhibits a core-shell structure with two different elemental dispersions which Au element is rich in the core while Pd element is rich in the shell, indicating the formation of the core-shell structural AuPd NPs. Evidently, the Pd shell is coated selectively on the surface of Au NPs to form a Pd-Au-TiO₂ heterostructure nanocrystal on the surface of 3DOM-TiO₂. During the reduction process of the metal precursor mixed solution, Au core first formed and deposited on the 3DOM-TiO₂ surface, then Pd shell produced and coated on the Au surface. The above-mentioned reduction process in sequence is due to the difference of standard reduction potentials of the HAuCl₄ and PdCl₂ solution. The core-shell-type NPs promote synergistic effects in Au-Pd metals and improve the transfer efficiency of photogenerated electrons and the subsequent photocatalysis [56,57].

3.6. The results of XPS characterization

To observe the electronic states of AuPd NPs, the XPS spectra of Au 4f and Pd 3d regions for Au₄/3DOM-TiO₂, Au₃Pd₁/3DOM-TiO₂ and Pd₄/3DOM-TiO₂ catalysts were recorded and the corresponding results are shown in Fig. 7 and Table 3. As shown in Fig. 7A, the bands of binding energies located at 82.6 and 86.3 eV are related to the spin-orbit coupling Au 4f 7/2 and Au 4f 5/2, respectively. Deconvolution of the Au spectra indicates that metallic (Au⁰) and ionic Au species (Au⁺ and Au³⁺) are coexist. For Au₄/3DOM-TiO₂ catalyst, the surface percent of Au⁰ and Au^{&+} (Au⁺ and Au³⁺) species, calculated from the peaks area, are 73.8, 26.2%, respectively. Moreover, after introduction of Pd species on the surface of Au/3DOM-TiO₂ (Au₃Pd₁/3DOM-TiO₂), the percent of Au^{&+} species increase from 26.2% to 31.8%. It is deduced that the core-shell structural AuPd NPs can decrease in the d-electron density of the Au atoms. As shown in Fig. 7B, the bands of binding energies corresponding to the spin-orbit coupling Pd 3d 5/2 and Pd 3d 3/2 are located at 334.2 and 339.7 eV, 335.4 and 341.0 eV, 337.0 and 342.4 eV, which are assigned to Pd⁰, Pd²⁺ and Pd⁴⁺ species, respectively. It indicates that both metallic (Pd⁰) and ionic Pd (Pd^{&+^a}: Pd²⁺ and Pd⁴⁺) species exist on the surface of 3DOM-TiO₂. For Pd₄/3DOM-TiO₂ catalyst, the surface percent of Pd^{&+} species is 37.8%, while the value decreases to 29.0% for Au₃Pd₁/3DOM-TiO₂ catalyst. It is associated with the electron transfer from Au⁰ to Pd^{&+} in core-shell structured AuPd NPs, thus, the percent of Au^{&+} species increase while the value of Pd^{&+} species decreases. Au^{&+} and Pd^{&+} species acting as electron trapping centers of photoexcited TiO₂ under light illumination, and the vectorial electron transfer from Au to Pd can further decrease the recombination rates of photogenerated charges. The chemical state of active metals may be conducive to the photocatalytic activity for the reduction of CO₂ with H₂O.

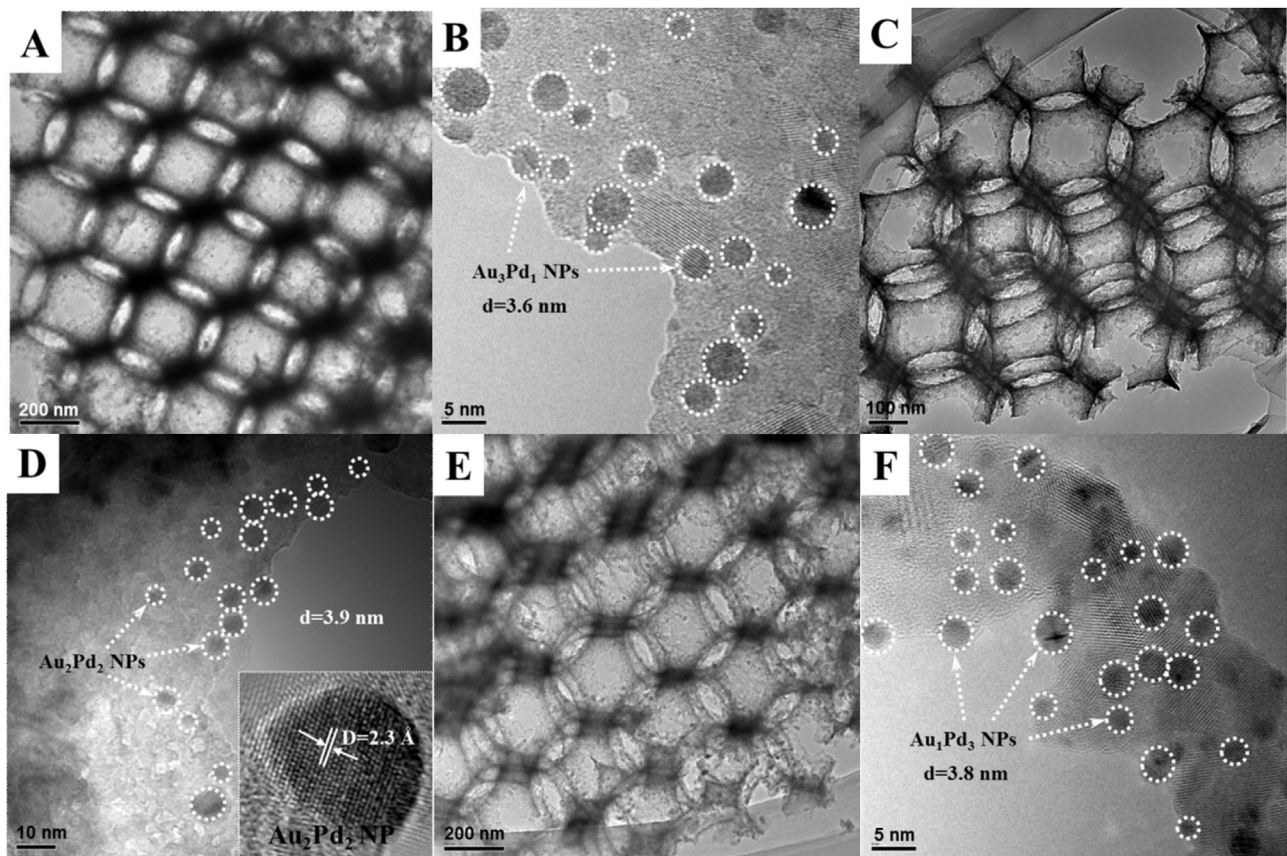


Fig. 5. TEM and HRTEM images of AuPd nanoparticles of AuPd/3DOM-TiO₂ catalysts. The one in HRTEM image of (D) shows an enlarged Au₂Pd₂ nanoparticles. A-B. Au₃Pd₁/3DOM-TiO₂; C-D. Au₂Pd₂/3DOM-TiO₂; E-F. Au₁Pd₃/3DOM-TiO₂.

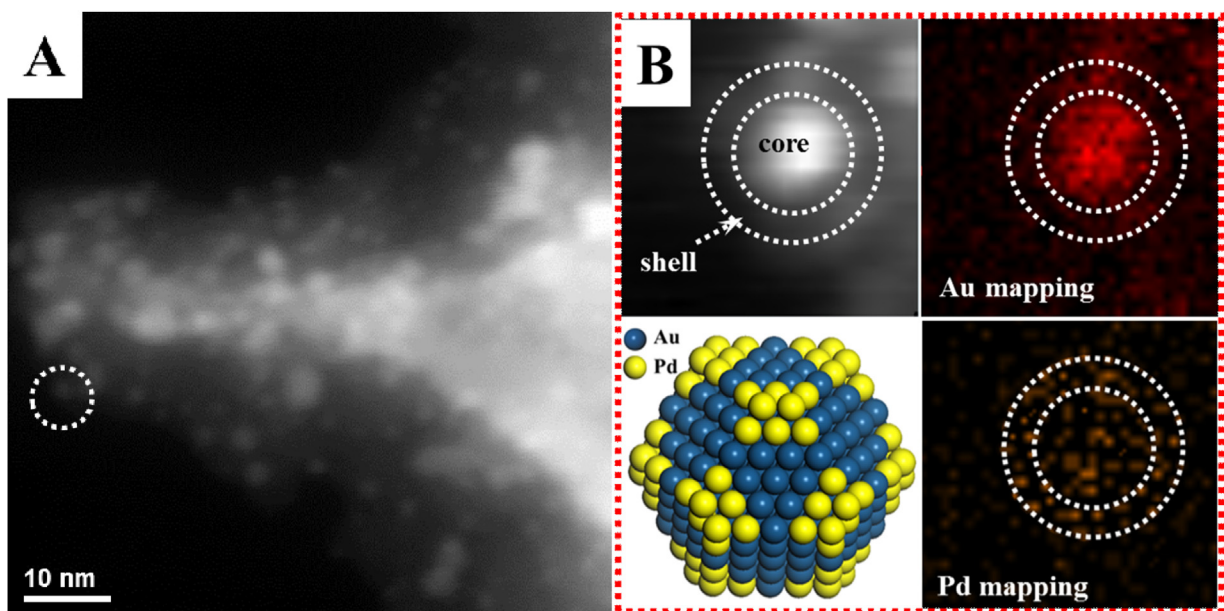


Fig. 6. HAADF-STEM (A) and EDS elemental mapping (B) images of Au₃Pd₁/3DOM-TiO₂ catalyst. And the model of Au₃Pd₁ nanoparticle is shown in Fig. B.

3.7. The results of UV–Vis diffuse reflectance spectroscopy (DRS) characterization

Fig. 8 shows the UV–Vis optical absorption spectra of 3DOM-TiO₂ and AuPd/3DOM-TiO₂ catalysts. The photoresponse of commercial P25 is limited in UV range due to its wide band gap

(~3.2 eV). 3DOM-TiO₂ support exhibits a wider light absorption region in comparison with the commercial P25, owing to the slow photon effect and multiple scattering of the 3DOM structure. As the light reflection spectra (Fig. 8A-a), the Bragg reflection peak value relative to the photonic stop-band is about 300 nm, and its red-edge centers at about 430 nm, which is overlapped with the electronic

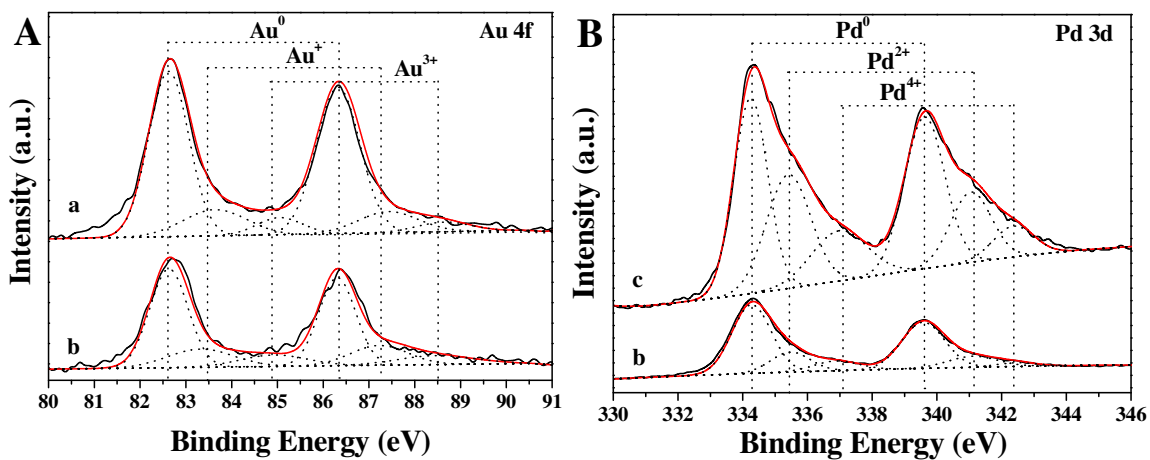


Fig. 7. XPS of Au 4f (A) and Pd 3d (B) regions of AuPd/3DOM-TiO₂ catalysts. a. Au₄/3DOM-TiO₂; b. Au₃Pd₁/3DOM-TiO₂; c. Pd₄/3DOM-TiO₂.

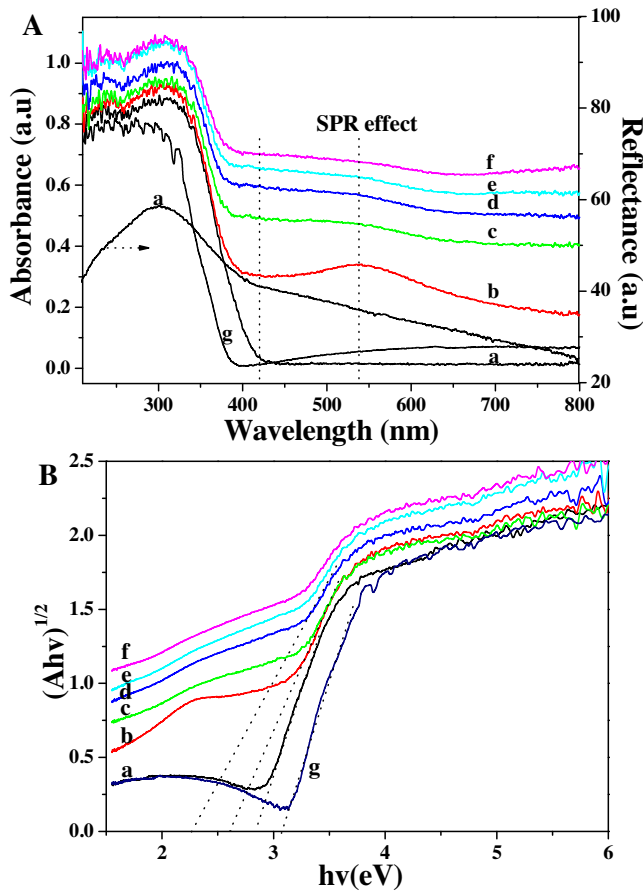


Fig. 8. UV-Vis DRS (A) and Kubelka-Munk transformed reflectance spectra (B) of 3DOM-TiO₂ and AuPd/3DOM-TiO₂ catalysts. (A) Shows simultaneously the absorbance spectra of 3DOM-TiO₂ and AuPd/3DOM-TiO₂ catalysts (Left) and the reflectance spectrum of 3DOM-TiO₂ photonic crystal film with stop band maxima at 300 nm (Right) a. TiO₂; b. Au₄/3DOM-TiO₂; c. Au₃Pd₁/3DOM-TiO₂; d. Au₂Pd₂/3DOM-TiO₂; e. Au₁Pd₃/3DOM-TiO₂; f. Pd₄/3DOM-TiO₂; g. commercial-P25.

absorption band of TiO₂ (420 nm). In other words, the 'red edge' of the photonic band gap for 3DOM-TiO₂ with an average pore size of 200 nm is coupled to the electronic absorption edge of TiO₂ (420 nm). It is well known that the light waves undergo multiple scattering and travel with a strongly reduced group velocity in the closely photonic stop-band edges, which is referred to as slow light [58]. It would increase light absorption ability as well as

improve photocatalytic activity in theory. Moreover, it is worthy to note that AuPd/3DOM-TiO₂ catalysts extend the photoresponse from ultraviolet to visible region (450–700 nm) and make significant enhancement in absorbance compared with pure 3DOM-TiO₂, which is assigned to the SPR effect and the photosensitizing effect of supported Au (Pd) NPs. With increasing the weight ratios of Pd/Au, the relative intensity of absorption peak centered at 530 nm decreases, indicating Pd metals selectively deposition on the Au core and formation of core-shell structured AuPd NPs.

The band gaps of the semiconductors are closely related to the absorbed wavelength range and play an important role in determining its photo-activity. Therefore, Kubelka-Munk function by the linear equation $(\alpha h \nu)^{1/2} = A(h\nu - E_g)$ is applied and the results are shown in Fig. 8B, in which α , h , ν , A and E_g are the absorption coefficient, Planck constant, light frequency, a constant and band gap energy, respectively [59,60]. It indicates that the E_g values of AuPd/3DOM-TiO₂ catalyst (about 2.25–2.6 eV) are much smaller than that of 3DOM-TiO₂ supports (2.90 eV). The smaller band gap of semiconductor would extend the light absorption region, and may be as a promising photocatalyst for solar-driven applications.

3.8. The results of photoluminescence (PL) spectroscopy characterization

PL emission spectroscopy is frequently used to study the electron-hole recombination in semiconductor [61]. The intensity of PL emission spectra can explore the recombination of excited electrons and holes, and the low intensity is accord with the low efficiency of electron-hole recombination. [62] In other words, the higher the PL intensity is, the higher recombination is. PL spectra of 3DOM-TiO₂ and AuPd/3DOM-TiO₂ catalysts were carried out using the excitation wavelength (λ_{EX}) of 380 nm, and the results are shown in Fig. 9. It is observed clearly that the curves were similar with each other except for fluorescence intensity. The emission peak centered at 525 nm is assigned to the emission of electron-hole recombination in TiO₂. The peak intensity of commercial-P25 is highest, indicating that it is easy to the recombination of excited electrons and holes. 3DOM-TiO₂ catalyst shows the relatively lower intensity in comparison with commercial-P25, which is related to the photonic stop-band and the slow-light effect of 3DOM material [63,64]. In other words, the wavelength of emission spectra is located to near the photonic stop-band edges of 3DOM material, the slow-light effect can considerably increase the effective path length of emission spectra due to the coherent multiple scattering and the low group velocity of the light. Moreover, the peak intensity of AuPd/3DOM-TiO₂ catalysts obviously decreases compared with

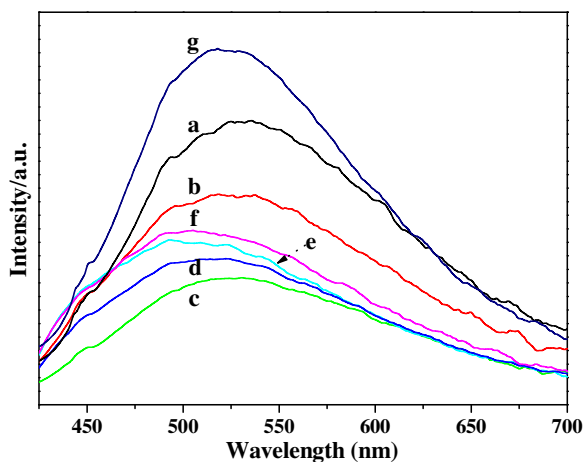


Fig. 9. PL spectra of 3DOM-TiO₂ and AuPd/3DOM-TiO₂ catalysts. a. TiO₂; b. Au₄/3DOM-TiO₂; c. Au₃Pd₁/3DOM-TiO₂; d. Au₂Pd₂/3DOM-TiO₂; e. Au₁Pd₃/3DOM-TiO₂; f. Pd₄/3DOM-TiO₂; g. commercial-P25.

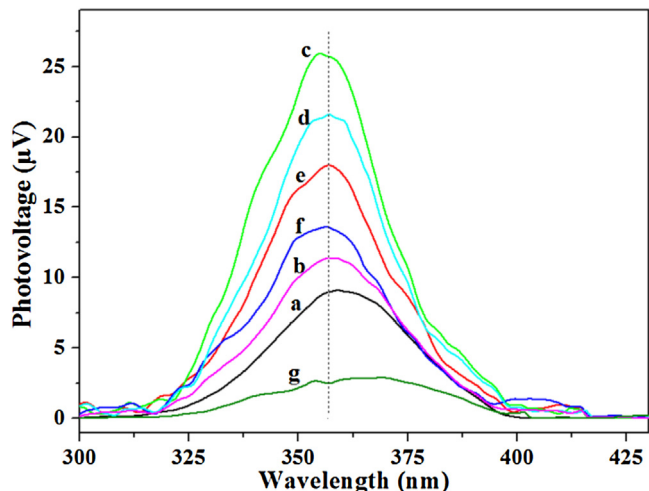


Fig. 10. SPV spectra of 3DOM-TiO₂ and AuPd/3DOM-TiO₂ catalysts. a. TiO₂; b. Au₄/3DOM-TiO₂; c. Au₃Pd₁/3DOM-TiO₂; d. Au₂Pd₂/3DOM-TiO₂; e. Au₁Pd₃/3DOM-TiO₂; f. Pd₄/3DOM-TiO₂; g. commercial-P25.

pure TiO₂ supports, which could be ascribed to the electron transfer from the conduction band of TiO₂ to bimetallic AuPd NPs. It indicates that the multi-coupling heterostructures of TiO₂-Au-Pd could reduce photo-generated electron-hole recombination by confining electrons in AuPd NPs while excited holes in VB of TiO₂. Among the catalysts, Au₃Pd₁/3DOM-TiO₂ catalyst shows the lowest intensity, thus, the suitable ratios of Au/Pd can efficiently improve the separation efficiency of excited charges and would enhance photocatalytic activity consequently.

3.9. The results of surface photovoltage (SPV) characterization

SPV measurement is another technique to reveal the separation efficiency of photogenerated electron-hole pairs, thus, the SPV spectra of 3DOM-TiO₂ and AuPd/3DOM-TiO₂ catalysts were measured and the results are shown in Fig. 10. The intensity of SPV signal was ascribed to the changes in the surface voltage before and after illumination, and the changes could be modulated by the charge separation [65]. The relatively high SPV signal means the high efficiency separation of the photo-generated charge carriers [66]. As depicted in Fig. 10, AuPd/3DOM-TiO₂ catalysts show a much higher SPV signal than that of pure 3DOM-TiO₂ support,

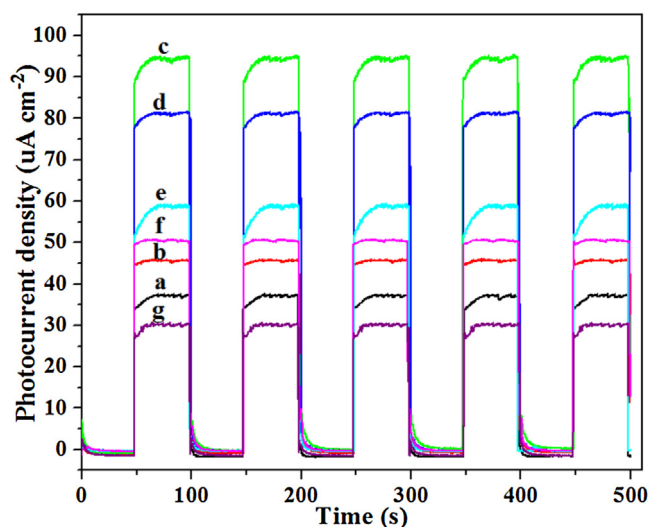


Fig. 11. Transient photocurrent responses of 3DOM-TiO₂ and AuPd/3DOM-TiO₂ catalysts. a. TiO₂; b. Au₄/3DOM-TiO₂; c. Au₃Pd₁/3DOM-TiO₂; d. Au₂Pd₂/3DOM-TiO₂; e. Au₁Pd₃/3DOM-TiO₂; f. Pd₄/3DOM-TiO₂; g. commercial-P25.

which is ascribed to the synergistic effect of supported AuPd NPs on the separation efficiency of illumination-induced electrons and holes. Moreover, Au₃Pd₁/3DOM-TiO₂ catalyst exhibits the highest SPV response, indicating the best separation efficiency of photoinduced electron-hole pairs, which is in agreement with the results of PL characterization. In the process of light irradiation, the conduction band electrons in TiO₂ are generated and then transferred to AuPd NPs, but the holes left in the valence band of TiO₂. The electron-sink function of supported AuPd NPs would be beneficial to the charge separation of photoexcited TiO₂ and would enhance photocatalytic activity.

3.10. The results of transient photocurrent characterization

It is well known that the transient photocurrent response induced by the incident light can reflect the number of separated charge carriers on the surface of photocatalysts [67]. The higher the photocurrent response is, the larger charge carrier number is [68]. In order to further illustrate the capability of supported AuPd NPs for promoting separation efficiency of photoinduced electron-hole pairs in AuPd/3DOM-TiO₂ photocatalytic system, the transient photocurrent responses under several on/off UV light irradiation cycles were performed, and the results are showed in Fig. 11. The photocurrent increased immediately when the light irradiation turns on, while it rapidly decreased to zero when the light was off. The photocurrent density of 3DOM-TiO₂ support is higher than commercial-P25, indicating the relatively high enrichment degree of photogenerated charges due to the slow light effect of 3DOM structure. Moreover, the transient photocurrent densities of bimetallic AuPd/3DOM-TiO₂ catalysts are higher than those of Au₄/3DOM-TiO₂ and Pd₄/3DOM-TiO₂ catalysts, demonstrating that the photoinduced electrons and holes in AuPd/3DOM-TiO₂ catalysts prefer to separate and transfer to surface rapidly. Au₃Pd₁/3DOM-TiO₂ catalyst shows the highest photocurrent density, indicating that it has the most effective separation rate of the photoinduced electrons. The weight ratios of Au/Pd can optimize the separation efficiency of photo-induced charges in TiO₂ in consistent well with the results of PL and SPV experiments.

In addition, in order to further verify the role of supported AuPd nanoparticles, the experiments of photocurrent response assigned to CO₂ reduction under the negative potential were also carried out and the results are shown in Fig. S3. A clear CO₂

reduction current was detected at the applied potential in aqueous solution under simulated sunlight. It is obviously noted that the photocurrent values decreased to the more negative position under the light irradiation in comparison with those without light. The values of transient photocurrent over bimetallic AuPd/3DOM-TiO₂ catalysts are more negative than those over Au₄/3DOM-TiO₂ and Pd₄/3DOM-TiO₂ catalysts, indicating that supported AuPd nanoparticles contribute to the enhancing transfer of electrons under the negative potential. Among the studied catalysts, the photocurrent value of Au₃Pd₁/3DOM-TiO₂ catalyst is the most negative, indicating that it has the most effective separation rate of the photoinduced electrons. During several light irradiation cycles, all samples display a relatively stable photocurrent response within several on/off cycles suggesting their good stabilities. All the observations highlight the excellent performance of 3DOM-TiO₂-supported bimetallic AuPd NPs catalysts for enhancing charge transfers in the photoreduction of CO₂ with H₂O system.

3.11. Photocatalytic reduction of CO₂

Prior to the activity tests for the photocatalytic reduction of CO₂, a series of preliminary tests were carried out in the absence of photocatalysts, or light irradiation, or CO₂ gas. Nevertheless, carbonaceous compounds were not observed in all cases. In order to verify the sources of carbon and hydrogen in the products of CO and CH₄, the analyses of ¹³C and ²H(D) isotopic tracing for the products of photocatalytic ¹³C-labeled CO₂ reduction with D₂O over Au₃Pd₁/3DOM-TiO₂ catalyst were carried out by means of GC-MS after 14 h irradiation and the results are shown in Fig. S4. It shows that the peak with *m/z* of 21 can be recognized as ¹³CD₄, and the peak with *m/z* of 29 can be attributed to ¹³CO. It indicates that the carbon (C) element in the product of CO and CH₄ comes from CO₂ reactant, and the hydrogen (H) element in the product of CH₄ come from H₂O reactant. Therefore, it is asserted that the reactants of CO₂ and H₂O are source to photocatalytic products (CO and CH₄), and both photocatalysts and light irradiation must be required for the reaction process of photocatalytic CO₂ reduction with H₂O.

The photocatalytic performances of as-prepared catalysts for CO₂ reduction are shown in Fig. 12 and Table 4. The production amount of CO₂ and CH₄ over 3DOM-TiO₂ support is larger than that of commercial P25, which is attributed to the slow photon effect of 3DOM structure for enhancing the light harvesting efficiency. The selectivity of CO production (*S*_{CO}) is higher than that of CH₄ production (*S*_{CH₄}), suggesting that, the productions derived from CO₂ reduction prefer to formation of CO rather than CH₄. Supported Au NPs on 3DOM-TiO₂ support can efficiently promote the selective formation of CH₄ and inhibit the CO production, and its *S*_{CH₄} value is 95.08%. After introduction of supported Pd NPs on 3DOM-TiO₂, the photocatalytic activity for CO₂ reduction with H₂O is improved obviously, i.e., the total formation rate of CH₄ and CO productions increases from 4.6 to 14.0 μmol g⁻¹ h⁻¹, and its formation rate of CO production is fastest (3.9 μmol g⁻¹ h⁻¹). Interestingly, AuPd/3DOM-TiO₂ catalysts exhibit a significantly synergistic effect of Au and Pd on enhancing photocatalytic activity for CO₂ reduction. Among the catalysts, Au₃Pd₁/3DOM-TiO₂ catalyst exhibits the highest efficiency for formation CH₄ (18.5 μmol g⁻¹ h⁻¹) and its *S*_{CH₄} value is 93.91%. The formation rate of CH₄ over Au₃Pd₁/3DOM-TiO₂ catalyst is about 11, 3, 1.8 times as high as that of 3DOM-TiO₂, Au₄/3DOM-TiO₂ and Pd₄/3DOM-TiO₂ catalysts, respectively. It is attributed to that AuPd NPs can promote electron transfer from TiO₂ to Au-Pd surface due to the lower Fermi level, and the synergistic effect of Au and Pd can enhance the separation efficiency of photogenerated electron-hole pairs. With the decreasing weight ratios of Au/Pd, the formation rate of CH₄ decreases and the evolving rate of CO increases, indicating that the excess deposition of Pd

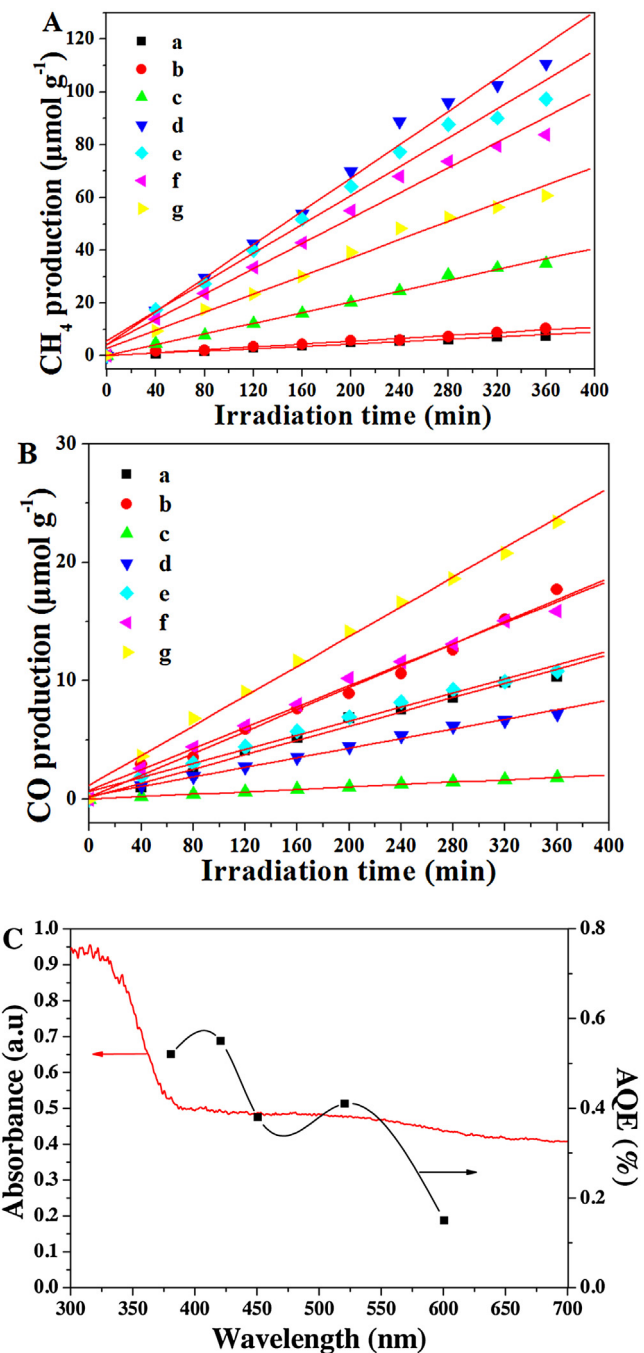


Fig. 12. Evolutions of CH₄ (A) and CO (B) production for photocatalytic conversion of CO₂ with H₂O over 3DOM-TiO₂ and AuPd/3DOM-TiO₂ catalysts. And comparison between UV-Vis DRS (Left) and action spectrum (Right) of Au₃Pd₁/3DOM-TiO₂ catalyst (C). a. commercial-P25; b. TiO₂; c. Au₄/3DOM-TiO₂; d. Au₃Pd₁/3DOM-TiO₂; e. Au₂Pd₂/3DOM-TiO₂; f. Au₁Pd₃/3DOM-TiO₂; g. Pd₄/3DOM-TiO₂.

on Au core can suppress the reduction of CO₂ to CH₄ and preferentially accelerate the reduction of CO₂ to CO.

For semiconductor-based photocatalytic reaction, the apparent quantum efficiency (AQE) is one of the most important parameters, which represents the conversion efficiency of the incident light to the desired product. In the photoreduction of CO₂ with H₂O reaction, the quantum efficiency can be calculated based on two electrons used for CO production and eight electrons used for CH₄ molecule and moles of photons input energy over the catalyst surface. As shown in Table 4, the AQE values of the as-prepared catalysts at wavelength of 520 nm were obtained. The AQE value

Table 4

The formation rates, the selectivity of CO and CH₄ productions and the apparent quantum efficiency (AQE) for photocatalytic conversion of CO₂ with H₂O over 3DOM-TiO₂ and AuPd/3DOM-TiO₂ catalysts.

| Sample | Formation rate [$\mu\text{mol g}^{-1} \text{h}^{-1}$] ^a | | | | S _{CO} (%) ^b | S _{CH₄} (%) ^b | AQE (%) ^d |
|--|--|-----|-------------------|-------------------|----------------------------------|--|----------------------|
| | CH ₄ | CO | H ₂ | O ₂ | | | |
| P25 | 1.3 | 1.8 | N.d. ^c | N.d. ^c | 58.06 | 41.94 | 0.04 |
| 3DOM-TiO ₂ | 1.7 | 2.9 | N.d. | N.d. | 63.04 | 36.96 | 0.05 |
| Au ₄ /3DOM-TiO ₂ | 5.8 | 0.3 | 63.9 | 47.6 | 4.92 | 95.08 | 0.19 |
| Au ₃ Pd ₁ /3DOM-TiO ₂ | 18.5 | 1.2 | 18.6 | 57.6 | 6.09 | 93.91 | 0.41 |
| Au ₂ Pd ₂ /3DOM-TiO ₂ | 16.2 | 1.8 | 16.8 | 53.3 | 10.00 | 90.00 | 0.37 |
| Au ₁ Pd ₃ /3DOM-TiO ₂ | 14.0 | 2.6 | 19.5 | 49.3 | 15.66 | 84.34 | 0.32 |
| Pd ₄ /3DOM-TiO ₂ | 10.1 | 3.9 | 20.1 | 46.15 | 27.86 | 72.14 | 0.16 |

^a Reaction conditions: photocatalyst, 0.1 g; CO₂ pressure, 0.1 MPa; H₂O, 2.0 mL; light source, 320–780 nm; irradiation time, 6 h; reaction temperature, 4 °C.

^b Based on the ratio of [CO] or [CH₄] amounts to sum ([CO]+[CH₄]) amounts.

^c Not determined.

^d The apparent quantum efficiency with irradiation light of 520 nm.

of 3DOM TiO₂ (0.05%) is higher than that of P25 (0.04%), indicating that 3DOM Ti-based catalyst is a high efficiency photocatalytic system for CO₂ reduction and 3DOM structure can obviously improve the light harvesting efficiency. Among the catalysts, the AQE value of Au₃Pd₁/3DOM-TiO₂ catalyst is 0.41% which is the largest value of light harvesting efficiency. Therefore, it is concluded that the suitable ratios of Au/Pd on the surface of 3DOM-TiO₂ is beneficial to CO₂ reduction and can enhance the formation rate of CH₄.

Based on the results of AQE values at different wavelength (380, 420, 450, 520 and 600 nm), the action spectrum of Au₃Pd₁/3DOM-TiO₂ catalyst was obtained and the result is shown in Fig. 12C. Meanwhile, the UV–Vis DRS spectrum is also presented in Fig. 12C. The AQE value of Au₃Pd₁/3DOM-TiO₂ catalyst increases with the increasing of light absorption, and the AQE value at 420 nm is the largest due to the slow photon effect of Au₃Pd₁/3DOM-TiO₂ for enhancing the light-harvesting efficiency. The relatively smaller AQE value at 380 nm, compared with at 420 nm, can be attributed to the suppression from the photonic band gap reflection in the light-harvesting efficiency. It is noted that the AQE value at 520 nm has an enhanced effect, which is assigned to the surface plasmon resonance effect of supported AuPd nanoparticles. Therefore, the enhancement in the photocatalytic efficiency of AuPd/3DOM-TiO₂ catalysts under light irradiation could be attributed to the combined action of the slow photon effect and the surface plasmon resonance effect.

Moreover, in order to verify the ratiocination, the formation rates of O₂ and H₂ over AuPd/3DOM-TiO₂ catalysts were further evaluated and the results are listed in Table 4. There is no doubt that Au₃Pd₁/3DOM-TiO₂ catalyst exhibits the highest formation rate of O₂ ($57.6 \mu\text{mol g}^{-1} \text{h}^{-1}$), which is larger than the stoichiometric theoretical amount ($46.9 \mu\text{mol g}^{-1} \text{h}^{-1}$) calculated by the formation rates of CH₄, H₂ and CO. Therefore, some others hydrocarbon products may be theoretically produced but undetected.

In order to investigate the stability of Au₃Pd₁/3DOM-TiO₂ catalyst, the experiments were repeated for five times under the same reaction condition. As shown in Fig. 13, Au₃Pd₁/3DOM-TiO₂ catalyst exhibits no obvious decrease in catalytic activities during five test cycles. Moreover, its macroporous structure and AuPd particle sizes did not change based on the analysis of SEM (Fig. S5), and TEM (Fig. S6). The circulation experiment verifies the well stability of the photocatalysts of AuPd NPs decorated on 3DOM-TiO₂.

4. Discussion

For the semiconductor photocatalysts, their relative positions of conduction band (CB) and valence band (VB) must meet the energy band theory for photoreduction of CO₂ to CO and CH₄ [69]. The photogenerated electrons can be just consumed when the CB of photocatalyst lies above the reduction potential of

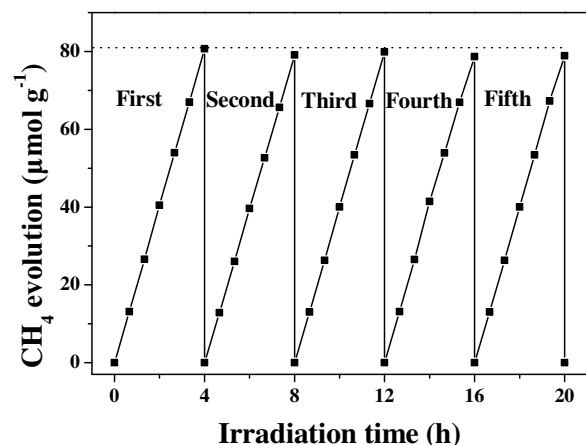
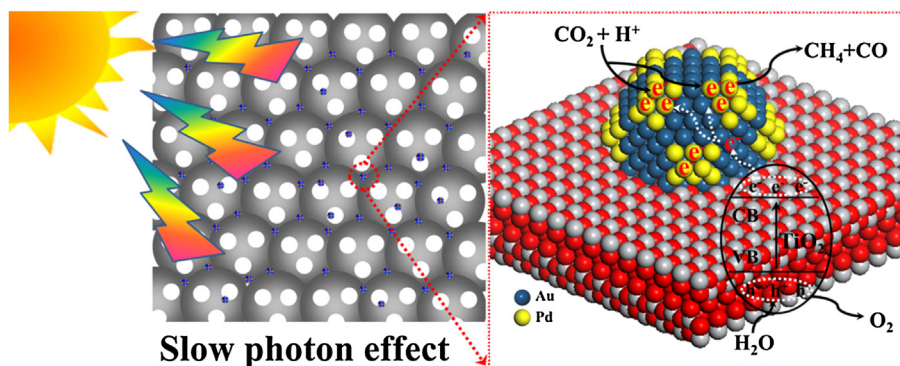


Fig. 13. Stability study on the evolution of CH₄ production over Au₃Pd₁/3DOM-TiO₂ catalyst for five test cycles.

CO₂/CH₄, CO₂/CO. The CB potential (E_{CB}) of TiO₂ is -0.56 V (vs. NHE at pH 7) [70], while the potentials of $E^0(\text{CO}_2/\text{CO}) = -0.53 \text{ V}$ and $E^0(\text{CO}_2/\text{CH}_4) = -0.24 \text{ V}$ are less negative than the E_{CB} of TiO₂ [71], thus, the reduction reactions of photoreduction CO₂ with H₂O to produce CO and CH₄ are theoretically feasible. In fact, the selective formation of CH₄ or CO is the result of the compromise between charge transfer and thermodynamics. The value of $E^0(\text{CO}_2/\text{CH}_4)$ is lower than that of $E^0(\text{CO}_2/\text{CO})$, in other words, the production of CH₄ is thermodynamically more feasible than the generation of CO if the supply of protons and electrons is high enough. However, from the view of charges, the production of one CH₄ molecule requires eight electrons and eight hydrogen protons, while the formation of one CO molecule just requires two electrons and two hydrogen protons. Thus, the production of CO is possible owing to the paucity of excited electrons [51,72,73]. But if enough protons and electrons were sufficiently afforded during the photocatalytic process, CH₄ would be the major reduction product [38,48]. The production rates and selectivity of CO and CH₄ in the gaseous product are related to the enrichment degree of electrons and hydrogen protons, which depends on the nanostructure and the surface property of photocatalysts.

Based on the results of photocatalytic CO₂ reduction with H₂O (Fig. 12 and Table 4), AuPd/3DOM-TiO₂ catalysts exhibit super catalytic performances. The enhanced photocatalytic activity for CO₂ reduction with H₂O can be isolated from the light-harvesting and charge-separation functions of the photocatalysts. For improving the light-harvesting, AuPd/3DOM-TiO₂ catalysts have two aspects. One aspect is attributed to the slow photon effect of 3DOM structure in accord with the results of our previous works [35,38,48,51]. The



Scheme 1. The catalytic mechanism for the photoreduction of CO_2 with H_2O over AuPd/3DOM-TiO₂ catalyst.

other aspect is the co-catalysts of core-shell structured AuPd NPs which can effectively extend the spectral response from UV to visible region. Based on the results of comparison between UV–Vis DRS and the action spectra of Au₃Pd₁/3DOM-TiO₂ catalyst (Fig. 12C), it is noted that the light-harvesting efficiency can be improved by the slow photon effect of 3DOM structure, and supported AuPd nanoparticles can further improve the absorption for visible light due to the surface plasmon resonance. Therefore, AuPd/3DOM-TiO₂ catalysts show the high photocatalytic efficiency under light irradiation.

For effective separation efficiency of the photogenerated charge carrier, it is mainly owing to the rapid interfacial charge transfer through the chemical heterostructure interactions and the synergistic effect of TiO₂ and noble metals (Au, Pd). On the one hand, the semiconductor of 3DOM-TiO₂ is excited to produce electron-hole pairs after the absorption of photons. From the results of XRD and Raman analysis (Fig. 3, Fig. 4), the crystal phase structures of anatase and rutile types are coexistent. The heterojunction of anatase/rutile phases would be formed in 3DOM TiO₂, and the anatase phase of TiO₂ shows the larger band gap (3.2 eV) and 0.1 eV higher Fermi level in comparison with those of rutile phase (3.0 eV) [74,75]. Thus, the photo-generated electrons may be transferred from anatase phase to rutile phase and consequently improve the separation efficiency of photo-generated electron-hole pairs. Then, the generated electrons in the CB of 3DOM-TiO₂ flow into Au, i.e., electron transfers from 3DOM-TiO₂ to AuPd. Then the enrichment electrons on the surface of AuPd NPs would be used for CO₂ reduction. The elementary steps of reduction proceeds involve the transfer of an electron, a proton, or hydrogen radical (H^\bullet), as well as breaking C–O bonds and creating new C–H bonds. On the other hand, the photo-generated holes (h^+) are left on the VB of TiO₂ semiconductor and are used to oxidize H₂O and formation of surface-bound hydrogen ions (H^+) and O₂. The mechanistic details for the conversion of CO₂ to CH₄ have not been fully elucidated, but three full pathways, such as the formaldehyde pathway, the carbene pathway and the glyoxal pathway, have been proposed in the literatures [17]. For co-catalysts with metal NPs, they are beneficial to facilitating CO₂ activation and improving charge separation for the reduction process. Combined the results of PL spectra (Fig. 9), the surface photovoltage (Fig. 10), the photocurrent action spectra (Fig. 11) and catalytic activity (Fig. 12, Table 4), the Au₃Pd₁/3DOM-TiO₂ catalyst shows the lowest recombination efficiency of photoinduced electron-hole pairs and the highest catalytic activity for CO₂ reduction.

Based on the discussion above, the mechanism for the photoreduction CO₂ with H₂O over AuPd/3DOM-TiO₂ catalysts is proposed and vividly shown in Scheme 1. Firstly, under light irradiation, the slow photon effect of 3DOM-TiO₂ sufficiently improves the light-harvesting efficiency. And after deposition AuPd NPs on TiO₂

supports, the absorbance for visible light is further enhanced remarkably due to the SPR and photosensitizing effect. Secondly, the excited electron-hole pairs in TiO₂ are generated after absorbing photons with energy equals to or greater than its bandgap. The coexistence of the anatase/rutile crystal phases in 3DOM TiO₂ can form the heterojunction of anatase/rutile phases, which can improve the separation efficiency of photo-generated electron-hole pairs. Then excited electrons transfer to Au NPs because of the different Fermi levels between Au and the CB edge of TiO₂. And then the vectorial electrons further transfer from Au to Pd, which decreases the recombination rates of photogenerated electron-hole pairs due to the electron trapping role of Au^{&+} and Pd^{&+} species and the surface plasmon resonance of Au NPs. In addition, at the interface of AuPd and TiO₂, the potential gradient established by the Schottky barrier suppresses the generated electrons getting back to TiO₂ once again. But the photogenerated holes are left on the VB of TiO₂ semiconductor. Eventually, the photoinduced electron-hole pairs were effectively separated through this way. And photoreduction of CO₂ and oxidation reaction proceed in loading noble metals and TiO₂ semiconductor separately. Active electrons assemble on AuPd NPs react with the adsorbed CO₂ to form CH₄ or other carbon containing compounds, while photogenerated holes enrich on the VB of TiO₂ and oxidize H₂O to produce surface-bound hydrogen ions (H^+) and O₂. During photocatalysis process, core-shell structured AuPd NPs not only provides the reduction sites but also serves as the electron sinks, leading to an effective charge separation and enhancement in photocatalytic activity. In a word, AuPd/3DOM-TiO₂ catalysts, which take both advantages of the high light-harvesting efficiency and the excellent separation of photogenerated charge carriers, exhibit superior photocatalytic performance for CO₂ reduction.

5. Conclusions

The novel photocatalysts of bimetallic AuPd NPs decorated 3DOM TiO₂ were fabricated by the GBMR method. AuPd/3DOM-TiO₂ photocatalysts possess well-defined 3DOM structure, and the core-shell structural AuPd NPs with uniform sizes (about 3.7 nm) homogeneously dispersed on the inner wall of carriers. The enhanced photocatalytic activity may originate from the excellent light-harvesting capacity and separation efficiency of photogenerated electrons and holes. The light-harvesting efficiency can be improved by the slow photon effect of 3DOM structural TiO₂ and the surface plasmon resonance of supported Au NPs. Moreover, the vectorial electron transfer of TiO₂ → Au → Pd induces a more efficient separation of photoinduced charges. AuPd/3DOM-TiO₂ catalysts exhibit excellent photocatalytic activity for CO₂ reduction with H₂O to CH₄ under light irradiation. The possible mechanism of photocatalytic CO₂ reduction with H₂O over AuPd/3DOM-TiO₂

catalysts is proposed. Our design and synthetic approach might be a great help in the design of more excellent photocatalysts.

Acknowledgements

This work is supported by the National Natural Science Foundation of China (No. 21673142 and 21477164), Beijing Nova Program (No. Z141109001814072), Specialized Research Fund for the Doctoral Program of Higher Education of China (No. 20130007120011).

Appendix A. Supplementary data

Supplementary data associated with this article can be found, in the online version, at <http://dx.doi.org/10.1016/j.apcatb.2017.02.076>.

References

- [1] F. Zuo, L. Wang, T. Wu, Z.Y. Zhang, D. Borchardt, P.Y. Feng, *J. Am. Chem. Soc.* 132 (2010) 11856–11857.
- [2] R.G. Li, F.X. Zhang, D.G. Wang, J.X. Yang, M.R. Li, J. Zhu, X. Zhou, H.X. Han, C. Li, *Nat. Commun.* 4 (2013) 1432.
- [3] A. Dhakshinamoorthy, S. Navalon, A. Corma, H. Garcia, *Energy Environ. Sci.* 5 (2012) 9217–9233.
- [4] E.V. Kondratenko, G. Mul, J. Baltrusaitis, G.O. Larrazabal, J. Perez-Ramirez, *Energy Environ. Sci.* 6 (2013) 3112–3135.
- [5] T. Inoue, A. Fujishima, S. Konishi, K. Honda, *Nature* 277 (1979) 637–638.
- [6] M. Tahir, N.S. Amin, *Appl. Catal. B* 162 (2015) 98–109.
- [7] S. Sato, T. Morikawa, T. Kajino, O. Ishitani, *Angew. Chem. Int. Ed.* 52 (2013) 998–992.
- [8] S. Zhou, Y. Liu, J.M. Li, Y.J. Wang, G.Y. Jiang, Z. Zhao, D.X. Wang, A.J. Duan, J. Liu, Y.C. Wei, *Appl. Catal. B* 20 (2014) 158–159.
- [9] H.G. Yang, C.H. Sun, S.Z. Qiao, J. Zou, G. Liu, S.C. Smith, H.M. Cheng, G.Q. Lu, *Nature* 453 (2008) 638–641.
- [10] S.J. Xie, Y. Wang, Q.H. Zhang, W.Q. Fan, W.P. Deng, Y. Wang, *Chem. Comm.* 49 (2013) 2451–2453.
- [11] S.C. Yan, S.X. Ouyang, J. Gao, M. Yang, J.Y. Feng, X.X. Fan, L.J. Wan, Z.S. Li, J.H. Ye, Y. Zhou, Z.G. Zou, *Angew. Chem. Int. Ed.* 49 (2010) 6400–6404.
- [12] S.B. Wang, X.C. Wang, *Appl. Catal. B* 162 (2015) 494–500.
- [13] Y. Ma, X.L. Wang, Y.S. Jia, X.B. Chen, H.X. Han, C. Li, *Chem. Rev.* 114 (2014) 9987–10043.
- [14] V.P. Indrakanti, J.D. Kubicki, H.H. Schobert, *Energy Environ. Sci.* 2 (2009) 745–748.
- [15] L.W. Zhang, H.B. Fu, Y.F. Zhu, *Adv. Funct. Mater.* 18 (2008) 2180–2189.
- [16] Q.Y. Zhang, T.T. Gao, J.M. Andino, Y. Li, *Appl. Catal. B* 123–124 (2012) 257–264.
- [17] S.N. Habisreutinger, L. Schmidt-Mende, J.K. Stolarczyk, *Angew. Chem. Int. Ed.* 52 (2013) 7372–7408.
- [18] T.C. An, J.Y. Chen, X. Nie, G.Y. Li, H.M. Zhang, X.L. Liu, H.J. Zhao, *ACS Appl. Mater. Interfaces* 4 (2012) 5988–5996.
- [19] J.L. Zhang, Y.M. Wu, M.Y. Xing, S.A.K. Leghari, S. Sajjad, *Energy Environ. Sci.* 3 (2010) 715–726.
- [20] M.Y. Wang, J. Ioccozia, L. Sun, C.J. Lin, Z.P. Lin, *Energy Environ. Sci.* 7 (2014) 2182–2202.
- [21] Y. Liu, S. Zhou, J.M. Li, Y.J. Wang, G.Y. Jiang, Z. Zhao, B. Liu, X.Q. Gong, A.J. Duan, J. Liu, Y.C. Wei, L.Q. Zhang, *Appl. Catal. B* 168 (2015) 125–131.
- [22] R.G. Li, Y.X. Weng, X. Zhou, X.L. Wang, Y. Mi, R.F. Chong, H.X. Han, C. Li, *Energy Environ. Sci.* 8 (2015) 2377–2382.
- [23] H.M. Zhang, P.R. Liu, X.L. Liu, S.Q. Zhang, X.D. Yao, T.C. An, R. Amal, H.J. Zhao, *Langmuir* 26 (2010) 11226–11232.
- [24] T. Kamegawa, S. Matsuura, H. Seto, H. Yamashita, *Angew. Chem. Int. Ed.* 52 (2013) 916–919.
- [25] S. Bera, J.E. Lee, S.B. Rawal, W.I. Lee, *Appl. Catal. B* 199 (2016) 55–63.
- [26] M. Klein, J. Nadolna, A. Gołębiewska, P. Mazierski, T. Klimczuk, H. Remita, A. Zaleska-Medynska, *Appl. Surf. Sci.* 378 (2016) 37–48.
- [27] J. Yan, Z.G. Chen, H.Y. Ji, Z. Liu, X. Wang, Y.G. Xu, X.J. She, L.Y. Huang, L. Xu, H. Xu, H.M. Li, *Chem-Eur. J.* 22 (2016) 4764–4773.
- [28] Y. Li, W.Q. Cui, L. Liu, R.L. Zong, W.Q. Yao, Y.H. Liang, Y.F. Zhu, *Appl. Catal. B* 199 (2016) 412–423.
- [29] T. Kamegawa, N. Suzuki, H. Yamashita, *Energy Environ. Sci.* 4 (2011) 1411–1416.
- [30] M. Wu, Y. Li, Z. Deng, B.L. Su, *ChemSusChem* 4 (2011) 1481–1488.
- [31] K.M. Ji, H.X. Dai, J.G. Deng, H.J. Zang, H. Arandiyan, S.H. Xie, H.G. Yang, *Appl. Catal. B* 168–169 (2015) 274–282.
- [32] L.W. Zhang, E. Reisner, J. Baumberg, *Energy Environ. Sci.* 7 (2014) 1402–1408.
- [33] J. Liu, G. Liu, M.Z. Li, W.Z. Shen, Z. Liu, J. Wang, J. Zhao, L. Jiang, Y. Song, *Energy Environ. Sci.* 3 (2010) 1503–1506.
- [34] J.I.L. Chen, G.A. Ozin, J. Mater. Chem. 19 (2009) 2675–2678.
- [35] Y.C. Wei, J.Q. Jiao, Z. Zhao, J. Liu, J.M. Li, G.Y. Jiang, Y.J. Wang, A.J. Duan, *Appl. Catal. B* 179 (2015) 422–432.
- [36] Y.C. Wei, J.Q. Jiao, Z. Zhao, W.J. Zhong, J.M. Li, J. Liu, G.Y. Jiang, A.J. Duan, J. Mater. Chem. A 3 (2015) 11074–11085.
- [37] J.Y. Chen, G.Y. Li, Y. Huang, H.M. Zhang, H.J. Zhao, T.C. An, *Appl. Catal. B* 123 (2012) 69–77.
- [38] J.Q. Jiao, Y.C. Wei, K.B. Chi, Z. Zhao, A.J. Duan, J. Liu, G.Y. Jiang, Y.J. Wang, X.L. Wang, C.C. Han, P. Zheng, *Energy Technol.* (2017), <http://dx.doi.org/10.1002/ente.201600572>.
- [39] F. Lin, D.G. Wang, Z.X. Jiang, Y. Ma, J. Li, R.G. Li, Can Li, *Energy Environ. Sci.* 5 (2012) 6400–6406.
- [40] F.L. Wang, Z.M. Jin, Y.J. Jiang, E.H.G. Backus, M. Bonn, S.N. Lou, D. Turchinovich, R. Amal, *Appl. Catal. B* 198 (2016) 25–31.
- [41] Q.G. Zhai, S.J. Xie, W.Q. Fan, Q.H. Zhang, Y. Wang, W.P. Deng, Y. Wang, *Angew. Chem. Int. Ed.* 52 (2013) 5776–5779.
- [42] B. Cao, G.S. Li, H.X. Li, *Appl. Catal. B* 194 (2016) 42–49.
- [43] H. Tada, T. Mitsui, T. Kiyonaga, T. Akita, K. Tanaka, *Nat. Mater.* 5 (2006) 782–786.
- [44] J.L. Zhang, Y. Lu, L. Ge, C.C. Han, Y.J. Li, Y.Q. Gao, S.S. Li, H. Xu, *Appl. Catal. B* 204 (2017) 385–393.
- [45] Z.Y. Zhang, S.W. Cao, Y.S. Liao, C. Xue, *Appl. Catal. B* 162 (2015) 204–209.
- [46] P.X. Liu, Y. Zhao, R.X. Qin, S.G. Mo, G.X. Chen, L. Gu, D.M. Chevrier, P. Zhang, Q. Guo, D.D. Zang, B.H. Wu, G. Fu, N.F. Zheng, *Science* 352 (2016) 797–800.
- [47] L.E. Wu, J. Gong, L. Ge, C.C. Han, S.M. Fang, Y.J. Xin, Y.J. Li, Y. Lu, *Int. J. Hydrogen. Energ.* 41 (2016) 14704–14712.
- [48] J.Q. Jiao, Y.C. Wei, Z. Zhao, W.J. Zhong, J. Liu, J.M. Li, A.J. Duan, G.Y. Jiang, *Catal. Today* 258 (2015) 319–326.
- [49] Y.C. Wei, Z. Zhao, T. Li, J. Liu, A.J. Duan, G.Y. Jiang, *Appl. Catal. B* 146 (2014) 57–70.
- [50] S.H. Xie, Y.X. Liu, J.G. Deng, X.T. Zhao, J. Yang, K.F. Zhang, Z. Han, H.X. Dai, *J. Catal.* 342 (2016) 17–26.
- [51] J.Q. Jiao, Y.C. Wei, Z. Zhao, J. Liu, J.M. Li, A.J. Duan, G.Y. Jiang, *Ind. Eng. Chem. Res.* 53 (2014) 17345–17354.
- [52] Y.C. Wei, J. Liu, Z. Zhao, A.J. Duan, G.Y. Jiang, *J. Catal.* 287 (2012) 13–29.
- [53] Z.H. Wang, Z.W. Tian, D.M. Han, F.B. Fu, *ACS Appl. Mater. Interfaces* 8 (2016) 5466–5474.
- [54] J. Fang, X. Bi, D. Si, Z. Jiang, W. Huang, *Appl. Surf. Sci.* 253 (2007) 8952.
- [55] M. Tahir, B. Tahir, N.A.S. Amin, *Appl. Catal. B* 204 (2017) 548–560.
- [56] M.L. Li, L.X. Zhang, X.Q. Fan, M.Y. Wu, M. Wang, R.L. Cheng, L.L. Zhang, H.L. Yao, J.L. Shi, *Appl. Catal. B* 201 (2017) 629–635.
- [57] Y.C. Wei, Z. Zhao, J. Liu, S.T. Liu, C.M. Xu, A.J. Duan, G.Y. Jiang, *J. Catal.* 317 (2014) 62–74.
- [58] X.Q. Chen, J.H. Ye, S.X. Ouyang, T. Kako, Z.S. Li, Z.G. Zou, *ACS Nano* 5 (43) (2011) 4310–4318.
- [59] W.Q. Fan, Q.H. Lai, Q.H. Zhang, Y. Wang, *J. Phys. Chem. C* 115 (2011) 10694–10701.
- [60] M. Yoon, M. Seo, C. Jeong, J.H. Kang, K.S. Jeon, *Chem. Mater.* 17 (2005) 6069–6079.
- [61] J. Tian, P. Hao, N. Wei, H.Z. Cui, H. Liu, *ACS Catal.* 5 (2015) 4530–4536.
- [62] Y.N. Tang, W.H. Di, X.S. Zhai, R.Y. Yang, W.P. Qin, *ACS Catal.* 3 (2013) 405–412.
- [63] R.C. Schrodin, M. Al-Daous, A. Stein, *Chem. Mater.* 13 (2001) 2945–2950.
- [64] X.S. Qu, H.W. Song, G.H. Pan, X. Bai, B. Dong, H.F. Zhao, Q.L. Dai, H. Zhang, R.F. Qin, S.Z. Lu, *J. Phys. Chem. C* 113 (2009) 5906–5911.
- [65] H. Wang, X. Quan, H.T. Yu, S. Chen, *Carbon* 46 (2008) 1126–1132.
- [66] D. Li, J.L. Jia, T. Zheng, X.W. Cheng, X.J. Yu, *Appl. Catal. B* 188 (2016) 259–271.
- [67] W. Zhou, W. Li, J.Q. Wang, Y. Qu, Y. Yang, Y. Xie, K.F. Zhang, L. Wang, H.G. Fu, D.Y. Zhao, *J. Am. Chem. Soc.* 136 (2014) 9280–9283.
- [68] H. Zhang, X. Quan, S. Chen, H.T. Yu, N. Ma, *Chem. Mater.* 21 (2009) 3090–3095.
- [69] H. Park, H. Kim, G.H. Moon, W.Y. Choi, *Energy Environ. Sci.* 9 (2016) 411–433.
- [70] S. Sakthivel, M.C. Hidalgo, D.W. Bahnemann, S.U. Geissen, V. Murugesan, A. Vogelzoh, *Appl. Catal. B* 63 (2006) 31–40.
- [71] E.E. Benson, C.P. Kubiak, A.J. Sathrum, J.M. Smieja, *Chem. Soc. Rev.* 38 (2009) 89–99.
- [72] W.N. Wang, W.J. An, B. Ramalingam, S. Mukherjee, D.M. Niedzwiedzki, S. Gangopadhyay, P. Biswas, *J. Am. Chem. Soc.* 134 (2012) 11128–111276.
- [73] J.L. White, M.F. Baruch, J.E. Pander III, Y. Hu, I.C. Fortmeyer, J.E. Park, T. Zhang, K. Liao, J. Gu, Y. Yan, T.W. Shaw, E. Abelev, A.B. Bocarsly, *Chem. Rev.* 115 (2015) 12888–12935.
- [74] J. Zhang, Q. Xu, Z.C. Feng, M.J. Li, C. Li, *Angew. Chem. Int. Ed.* 47 (2008) 1766–1769.
- [75] Y. Luo, X.Y. Liu, J.G. Huang, *CrystEngComm* 15 (2013) 5586–5590.